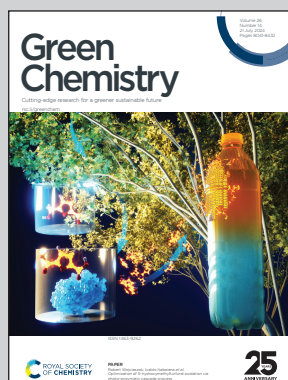


Showcasing research from Dr. Kothandaraman and co-workers, Pacific Northwest National Laboratory, Richland, WA, US.

Reactive direct air capture of CO₂ to C-C coupled products using multifunctional materials

A combined sorbent-catalytic material (Fe/K₂CO₃/Al₂O₃) has been developed for the Integrated Direct Air Capture and Catalytic (**iDAC-CAT**) process, which converts captured CO₂ from air into valuable C₂₊ products such as olefins. Herein, the proximity between K and Fe was identified as critical for producing C-C coupled products from the captured CO₂. Initial technoeconomic and life-cycle assessments suggest that the proposed iDAC-CAT technology can considerably lower DAC costs and potentially produce renewable olefins with negative greenhouse gas emissions.

As featured in:



See Jotheeswari Kothandaraman *et al.*, *Green Chem.*, 2024, **26**, 8242.



Cite this: *Green Chem.*, 2024, **26**, 8242

Reactive direct air capture of CO₂ to C–C coupled products using multifunctional materials†

Shazia Sharmin Satter, Johnny Saavedra Lopez, Michael L. Hubbard, Yuan Jiang, Robert A. Dagle and Jotheeswari Kothandaraman *[†]

Current direct air capture (DAC) approaches require a significant amount of energy for heating CO₂-sorbed materials for regeneration and for compressing CO₂ for transportation purposes. Rationally designing materials offering both capture and conversion functionalities could enable more energy and cost-efficient DAC and conversion. We have developed a single sorbent-catalytic (non-noble metal) material for the Integrated Direct Air Capture and CATalytic (iDAC-CAT) conversion of captured CO₂ into value-added products. Solid sorbents are integrated with catalytic components to first capture CO₂ from air. Subsequently, captured CO₂, with renewable H₂ co-feed is converted into olefins and paraffins. To the best of our knowledge, this is the first proof-of-concept demonstration for production of C₂ products such as olefins from captured CO₂. Among the different sorbent-catalytic materials studied, Fe/K₂CO₃/Al₂O₃ showed the best performance for integrated CO₂ capture and conversion to C₂ products. CO₂ capture capacity of 8.2 wt% was achieved under optimized capture conditions at 25 °C, and a conversion of >70% to paraffins and olefins was achieved at 320–400 °C. The hydrogenation of captured CO₂ was facilitated by the *in situ* formation of Fe₃O₄ and Fe₅C₂ species. The proximity between K and Fe was identified to be critical for producing C₂ products from the captured CO₂. The preliminary technoeconomic and life-cycle assessments suggest that the cost of the DAC can be considerably decreased by adopting the suggested iDAC-CAT technology, while renewable olefins could potentially be produced with negative greenhouse gases emissions.

Received 13th March 2024,
Accepted 13th May 2024
DOI: 10.1039/d4gc01244e
rsc.li/greenchem

Introduction

Given the increasing CO₂ concentration in the atmosphere, rapid and massive deployment of negative emission technologies (NETs) will be needed to limit global temperature increase to 1.5–2 °C.¹ NETs should be large enough to remove several gigaton quantities of CO₂ from the atmosphere and in this context, DAC is expected to complement other NET options. DAC technologies remove CO₂ from the atmosphere at any location to balance emissions that are unavoidable or technically difficult to avoid.² A variety of sorbents are being investigated for CO₂ capture, including physisorbents such as metal-organic frameworks,³ zeolites,^{4,5} and activated carbon,⁶ as well as chemisorbents such as amine-functionalized adsorbents that commonly contain polyamines.^{7,8} Particularly, chemisorbents are best suited for CO₂ capture from ultra-dilute sources such as air due to strong chemical interactions between CO₂ and sorbents. As a result, chemisorbents are the

subject of extensive studies aimed at understanding and improving their CO₂ adsorption and desorption processes. However, the economic feasibility of large-scale deployment of current DAC systems is uncertain due to high energy input needed for the desorption process (cost estimates are \$200–1000 per tonne CO₂ for DAC compared to \$36–53 per tonne CO₂ for coal-derived flue gas).⁹ Thus, innovative use opportunities, including synthetic fuels and chemicals are desired as a means to drive down costs and provide a market for DAC. However, there are no commercial technologies that can economically produce either value-added fuels and chemicals, or solid products for storage using CO₂ captured from air.

The capture of CO₂ and conversion of CO₂ have long been viewed as two independent processes. Recently, the benefits associated with integrating the capture and conversion processes have been realized by the scientific community.^{10–13} The direct conversion of captured CO₂ into value-added products (coupled approach) has potential advantages over traditional decoupled CO₂ capture and CO₂ conversion because the coupled approach avoids the energy-intensive sorbent regeneration (CO₂ desorption), compression and transportation steps. Importantly, new reactive pathways for the CO₂ conversion can be realized in the capture media, leading to

Pacific Northwest National Laboratory, Advanced Energy Systems, 902 Battelle Blvd, Richland, WA 99352, USA. E-mail: jotheeswari.kothandaraman@pnnl.gov

† Electronic supplementary information (ESI) available. See DOI: <https://doi.org/10.1039/d4gc01244e>



higher conversion, selectivity, and reduced cost.¹¹ For example, typical gas-phase CO₂ hydrogenation to methanol requires high temperatures due to slower kinetics. At high temperature, a competing reaction—the reverse water gas shift reaction—is also favored, which reduces the selectivity and consumes valuable H₂. On the other hand, in the amine-based capture medium, CO₂ hydrogenation to methanol followed a nontraditional route for conversion to methanol through a formamide intermediate.^{14–17} This nontraditional low-temperature methanol synthesis route was made possible by the presence of an amine-based capture solvent medium. However, amine-based aqueous/non-aqueous solvents are not suitable for DAC application due to high volatility, viscosity, and evaporative loss of water under realistic DAC conditions. For DAC, solid sorbents have several benefits (over well-studied liquid sorbents) such as increased adsorption capacities, lower regeneration energy penalties, relative ease of handling, and improved recyclability.^{18,19}

Though the feasibility of integrating capture and conversion processes has been shown with liquid capture solvent systems,^{11,14,17,20–23} the material design principles are not transferable to solids because unlike liquid systems, the sorbent and catalyst need to be integrated into a single multifunctional material in solids. The solid-state iDAC-CAT approach is limited by the lack of design parameters for this

multifunctional material with the cooperative sorbent and catalytic features to perform both capture and conversion. In traditional DAC approaches, solid or liquid sorbents with low reaction enthalpy, high capture capacity, and rapid kinetics are preferred. The strong binding of CO₂ *via* chemisorption is considered a limitation in traditional DAC approaches due to regeneration requirements. But in the iDAC-CAT approach, the strong binding will be considered an opportunity because the captured CO₂ is undergoing chemical conversion. The strong CO₂ binding will enhance the CO₂ uptake kinetics, which is critical for DAC application.

Solid materials with dual functionalities have been reported for integrated CO₂ capture and conversion to C₁ products such as methane^{24–30} and methanol.^{31–34} Most of these materials are composed of sorbents (metal oxides and carbonates) and metal catalysts (such as Ru, Ni, and Rh).^{35,36} In a first step, the sorbent reacts with CO₂ to form (bi)carbonate and in a second step, (bi)carbonate reacts with hydrogen at high temperature (>300 °C) to form methane. Most of these materials also require high temperature for capture, which is not an economical option.^{24,37–39} Amine-functionalized silica and Pd catalyst combinations have been demonstrated to be active for the integrated capture and conversion to methanol.^{32,33} Recently, Cu/Zn catalyst and metal carbonate combinations were identified as effective for the reactive capture of CO₂ to methanol.^{31,34} While these materials are effective for the formation of C₁ products, the conversion of captured CO₂ to C₂₊ products remains a challenge.

In this work, we report how combinations of catalytic components and sorbents can be integrated into a single material that can capture CO₂ from air at ambient conditions, and then convert the captured CO₂ into valuable C₂ products such as olefins. Olefins are building blocks for producing a variety of products including plastics, paints, lubricants, and surfactants. Olefins can also be converted into hard-to-decarbonize jet and diesel fuels.⁴⁰ In this work, Fe-based catalytic components were incorporated into the sorbent materials to facilitate the formation of C–C bonds. Upon studying different materials and conditions, we show a proof of concept using Fe/K₂CO₃/Al₂O₃ (Fe/KA) to produce C₂–C₄ olefins from CO₂ derived from air. We also identified that these materials are effective at converting gas-phase CO₂ to olefins, with olefin to paraffin ratio of 6.9 at 360 °C.



Jotheeswari Kothandaraman

full-time Scientist position at PNNL. She is interested in developing green and sustainable chemical processes for fuels and materials. Currently, she is leading projects on the upcycling of CO₂ sourced from both air and flue gas emissions. Dr Kothandaraman holds two US patents and has authored invited book chapters and perspective articles on CO₂ capture and conversion. Dr Kothandaraman's contributions have been recognized with the Phi Kappa Phi Award for Creative and Scholarly Achievements. In 2023, Dr Kothandaraman was elected Fellow of the Royal Society of Chemistry, and she also received the PNNL Laboratory Director's Award for Early Career Exceptional Achievement, also known as the Ronald L. Brodzinski Award. Currently, she serves as an advisory board member for the RSC Sustainability journal.

Dr Jothi Kothandaraman is a Scientist at the Pacific Northwest National Laboratory (PNNL), one of the US Department of Energy national laboratories. She obtained her Ph.D. in chemistry from the University of Southern California, focusing on catalytically driven reversible hydrogen storage materials. In 2017, she joined PNNL as a postdoctoral researcher, performing research on the catalytic conversion of CO₂. In 2019, she accepted a

Results and discussion

CO₂ capture studies using K₂CO₃/Al₂O₃

Inorganic chemisorbents are chosen for this study because they are more durable and low-cost materials compared to amine-based sorbents for DAC.⁴¹ The commonly used inorganic chemisorbents for DAC are CaO, MgO, and alkali metal carbonates.⁴² Among these sorbents, alkali metal carbonates can perform capture at ambient temperature.^{43,44} Alkali metal carbonates are usually dispersed on high-surface-area materials such as Al₂O₃, to increase the carbonation rate



of alkali carbonates.^{45,46} Based on literature studies conducted on K_2CO_3 loading on various supports, including carbon, alumina, and ZrO_2 , an optimal K_2CO_3 loading between 25–35 wt% on supports was identified for CO_2 capture. The adsorption capacity increases with higher K_2CO_3 loading; however, loading above 35 wt% results in decreased adsorption capacity due to reductions in surface area and pore volume.^{47–49} Thus, here 25 wt% of K_2CO_3/Al_2O_3 was synthesized,⁵⁰ characterized, and evaluated at 25 °C at different capture conditions to identify suitable conditions for DAC (sections S1.2, 1.3 and 1.4†). As-synthesized K_2CO_3/Al_2O_3 was characterized by BET (Brunauer–Emmett–Teller) analysis. Type IV isotherms with a characteristic hysteresis loop for both Al_2O_3 and K_2CO_3/Al_2O_3 were realized in the BET analysis (shown in Fig. S1A†), indicating that alumina is mesoporous in nature. Impregnation of K_2CO_3 over alumina resulted in a decrease in both surface area and pore volume of the original support, but the average pore sizes were almost comparable as shown in Table S1.† This implies that smaller sizes of K_2CO_3 filled the pores of the mesoporous alumina, confirming the dispersion of K_2CO_3 over the alumina surface.⁴⁴

The effect of pretreatment conditions and water vapor content on the capture performance of the sorbent was studied. The K_2CO_3/Al_2O_3 sorbent was first pretreated at 200 °C for 1 h under N_2 flow (100 mL min⁻¹). The material was then cooled to room temperature and pre-saturated with both 0.5 and 1.0 mol% H_2O vapor, followed by introduction of 400 ppm of CO_2 (Fig. S2A and S2B†) with H_2O vapor (0.5 or 1.0 mol%). The amount of CO_2 per g of sorbent adsorbed during both the experiments was calculated from the molar flow concentration profile of CO_2 versus time. For 0.5 mol% of H_2O , 850 $\mu\text{mol g}^{-1}$ of CO_2 was adsorbed, whereas in the case of 1.0 mol% of H_2O , 770 $\mu\text{mol g}^{-1}$ of CO_2 was adsorbed. This indicates that the 0.5 mol% of H_2O had a slightly higher adsorption capacity, possibly due to the K_2CO_3 phase transition in the presence of excess water.⁵¹

The effect of saturating the sorbent with water vapor during CO_2 capture was investigated. Here, CO_2 was co-fed with 0.5 mol% H_2O vapor over the pretreated K_2CO_3/Al_2O_3 as shown in Fig. S3† and compared with the pre-saturated sample (0.5 mol% H_2O vapor pretreatment). The water vapor co-fed sample shows the highest sorption capacity of 6.5 wt% compared to the water vapor pretreated samples, as shown in Fig. S3.† The amount of CO_2 adsorbed by the 25 wt% K_2CO_3/Al_2O_3 sorbent is ~6.5 wt%, surpassing the amounts reported in the literature, which are 3.6 wt% for K_2CO_3/Al_2O_3 and 4.1 wt% for K_2CO_3/Al_2O_3 –750 (Al_2O_3 heated at 750 °C before K_2CO_3 impregnation) under similar capture conditions, as shown in Table S3.†⁵² The increased CO_2 capture capacity could result from the fine dispersion of K_2CO_3 over Al_2O_3 . The X-ray diffraction (XRD) analysis shown in Fig. S1B† illustrates the change in phase composition of the K_2CO_3/Al_2O_3 before and after CO_2 capture at room temperature in the presence of water vapor. For fresh K_2CO_3/Al_2O_3 , the main diffraction peaks were attributed to dawsonite, $KAlCO_3(OH)_2$, K_2CO_3 , and $\gamma-Al_2O_3$. The formation of the dawsonite on the fresh samples

takes place due to the exposure of as-synthesized K_2CO_3/Al_2O_3 to CO_2 in air. This agrees with the Temperature Programmed Desorption (TPD) of the fresh material shown in Fig. S1C,† where the peak at 350 °C is due to the decomposition of the dawsonite.

Thermal decomposition of the CO_2 -captured K_2CO_3 using TPD shown in Fig. S1C† shows two characteristic peaks within 100–200 °C, which is likely due to the decomposition of the species containing bicarbonate, K_2CO_3 ·2KHCO₃·1.5H₂O, and KHCO₃. This agrees with the XRD diffraction patterns of the air-captured sorbent. The higher-temperature peak is mainly due to the decomposition of the $KAlCO_3(OH)_2$, which was reported to take place between 260 and 320 °C.⁴⁴

As activated carbon (AC) is recognized as a suitable support material for CO_2 capture, K_2CO_3/AC was synthesized and tested to evaluate its CO_2 capture capacity.⁴⁹ Compared to K_2CO_3/Al_2O_3 , the capture capacity of K_2CO_3/AC was 1.3 times lower, as shown in Fig. S4.† Due to the superior capture performance of K_2CO_3/Al_2O_3 under the optimized reaction conditions, K_2CO_3/Al_2O_3 was chosen as the sorbent material for the integrated capture and conversion studies.

Conversion of captured CO_2 to C_1 and C_2 products

The direct conversion of captured CO_2 from air or concentrated point sources to C_1 products such as methane, methanol, and CO has been effectively demonstrated in earlier studies.^{24–26,29–31,34,53} However, due to the high energy barrier of C–C coupling reactions, conversion of captured CO_2 to C_{2+} products is still a challenge. In the literature, combining the endothermic reverse water gas shift (RWGS) ($CO_2 + H_2 \rightarrow CO + H_2O$) reaction with the exothermic Fischer–Tropsch (FTS) ($CO + H_2 \rightarrow C_xH_y$) reaction has been identified as one of the strategies for converting concentrated streams of CO_2 and H_2 in the gas phase to C_{2+} products.⁵⁴ Particularly, potassium (alkali metal) modified Fe-based catalysts are known to promote carbon-chain growth in the gas-phase CO_2 hydrogenation reactions.^{55–58} We hypothesized that by combining the Fe-based catalysts and potassium-based sorbents the captured CO_2 can be directly converted to C_{2+} products, bypassing the energy-intensive CO_2 regeneration and compression steps. Additionally, alkali modification of metals can potentially develop optimal electronics that allow the selective formation of olefins by decreasing the reactivity of adsorbed H species.^{59,60} To test our hypothesis, we synthesized different combinations of iron and K_2CO_3/Al_2O_3 based sorbent-catalytic materials and evaluated the capture and conversion performance of these synthesized materials.

Fe₂O₃–K₂CO₃/Al₂O₃. A physical mixture of Fe_2O_3 and K_2CO_3 has been reported to be effective for converting CO_2 into C_2 – C_4 olefins with approximately 31% selectivity via a tandem mechanism.⁵⁶ The addition of K_2CO_3 is the key for promoting the formation of CO (via potassium bicarbonate and potassium formate intermediates), which gets converted into olefins and paraffins in the presence of iron oxide and iron carbide phases at 350 °C. Based on this study, we evaluated a physical mixture of Fe_2O_3 – K_2CO_3/Al_2O_3 (Fe_2O_3 –KA). The Fe_2O_3 –KA was



prepared as mentioned in section S1.2† and pretreated at 400 °C under H₂ flow (60 mL min⁻¹) for 5 h to convert Fe₂O₃ to Fe nanoparticles.

CO₂ capture was performed with 400 ppm of CO₂ (1200 mL min⁻¹) and 0.5 mol% of H₂O at 25 °C. The capture performance was compared with K₂CO₃/Al₂O₃, which was activated under similar conditions. Under this condition, ~100% of the K₂CO₃ was utilized during CO₂ capture in the case of K₂CO₃/Al₂O₃, whereas in the case of Fe₂O₃–KA, only 81% of the K₂CO₃ was utilized in CO₂ capture, as shown in Table S2.† High-temperature pretreatment enhanced the capture capacity through the dawsonite decomposition reaction.⁴⁴ Then, hydrogenation of the captured CO₂ was performed under hydrogen pressure of 1.0 MPa at 320 °C (hold for 2.5 h) and 360 °C (hold for 2 h) at a ramp rate of 5 °C min⁻¹ under H₂ flow (60 mL min⁻¹). This resulted in desorption of CO₂ with no detectable amount of hydrogenated CO₂-derived products. Most of the CO₂ was released at ~320 °C, suggesting that dawsonite is the major species formed during CO₂ capture.

K₂CO₃/Fe/C and K₂CO₃/Fe/C/Al₂O₃. Sun *et al.* showed that the use of potassium-promoter-modified Fe/C catalysts can

increase olefin selectivity in CO₂ hydrogenation.⁵⁷ Fe/C was synthesized by the hydrothermal method (section S1.2 in ESI†). K₂CO₃/Fe/C was formed by impregnating K₂CO₃ (25 wt%) on the Fe/C catalyst. The synthesized material was pretreated at 400 °C under H₂ flow for 10 h to ensure carbide formation before CO₂ capture and conversion studies.⁵⁷ CO₂ capture was performed by following the standard capture procedure mentioned in section S1.4.† The capture profile is shown in Fig. 1A. In the first 50 min, there was an induction period after which the CO₂ capture breakpoint started. The initial delay in the capture could either be due to physical adsorption of the CO₂ occupying the macropores of the materials or because the material surface was not immediately saturated with water vapor, which is necessary to start the carbonation reaction. The total CO₂ captured in 4 hours by this material typically ranges between 600 and 700 μmol g⁻¹, which is ~2 times lower than that of K₂CO₃/Al₂O₃ (see Table 1).

As shown in Fig. 1B, conversion of the captured CO₂ was carried out with H₂ feed at different temperatures. When the temperature was increased from room temperature (capture) to 320 °C (conversion) some unreacted CO₂ began to desorb.

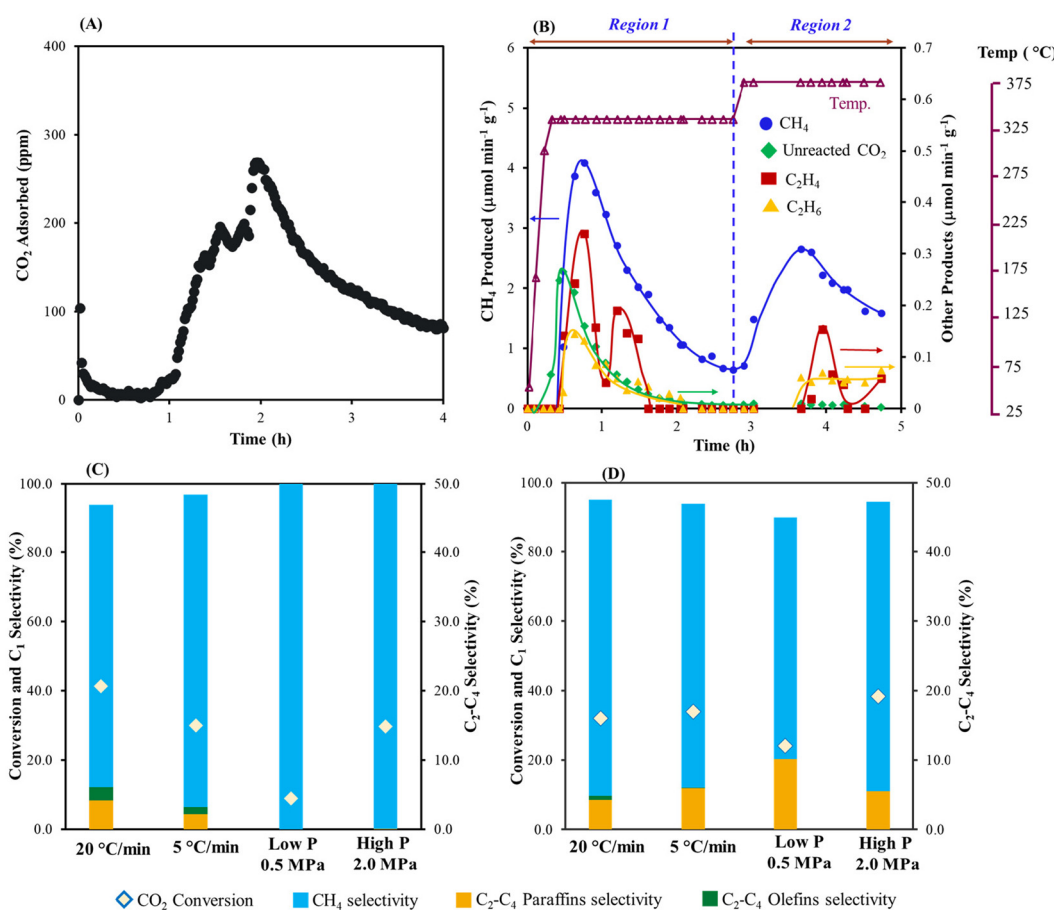


Fig. 1 (A) CO₂ capture profile over K₂CO₃/Fe/C at 25 °C, (B) hydrogenation profile of the captured CO₂ (at heating rate of 20 °C min⁻¹), (C) comparison of the CO₂ conversion and selectivity of products formed in Region 1, at 320 °C, and (D) comparison of the CO₂ conversion and selectivity of the products formed in Region 2, at 360 °C. Amount of material: 2 g; pretreatment conditions: H₂ = 60 mL min⁻¹, 400 °C, 10 h; CO₂ capture conditions: CO₂ = 400 ppm in N₂ (flow rate = 1200 mL min⁻¹), H₂O vapor = 0.5 mol%, 25 °C, 4 h; hydrogenation: H₂ = 60 mL min⁻¹, 1.0 MPa, 320 °C for 2.5 h (5 °C min⁻¹), followed by heating to 360 °C (5 °C min⁻¹) for 2 h. The selectivity of CO is <5% during the hydrogenation.

Table 1 Comparison of the physicochemical properties, CO_2 capture and catalytic activity

Entry	Materials	Physical properties		CO_2 capture		Catalytic activity					
		SA ($\text{m}^2 \text{g}^{-1}$)	PV ($\text{cm}^3 \text{g}^{-1}$)	Average diameter (nm)	($\mu\text{mol g}^{-1}$)	(wt%)	CO_2 conv. (%)	CH_4 sel (%)	$\text{C}_2\text{--C}_4$ paraffins sel (%)	$\text{C}_2\text{--C}_4$ olefins sel (%)	C_{5+} sel (%)
1	Fe/C	33.16	0.4008	— ^c	N/A	N/A	N/A	N/A	N/A	N/A	N/A
2	Al_2O_3	182.4	0.6001	11.4	N/A	N/A	N/A	N/A	N/A	N/A	N/A
3	$\text{K}_2\text{CO}_3/\text{Al}_2\text{O}_3$	99.19	0.3262	10.09	1862	8.2	N/A	N/A	N/A	N/A	N/A
4	$\text{K}_2\text{CO}_3/\text{Fe/C}^a$	—	—	—	600–700	2.6–3.1	30.0	96.8	2.2	1.0	0.0
5	$\text{K}_2\text{CO}_3/\text{Fe/C}^b$	—	—	—	—	—	41.4	93.9	4.1	2.0	0.0
6	$\text{K}_2\text{CO}_3/\text{Fe/C/Al}_2\text{O}_3^a$	29.23	0.2476	8.95	1223	5.4	30.5	83.2	8.6	7.3	0.9

Pretreatment conditions for materials: $\text{H}_2 = 60 \text{ mL min}^{-1}$, 400°C , 5 h (entry 3) and 10 h (for entries 4–6); CO_2 capture conditions: $\text{CO}_2 = 400 \text{ ppm}$ in N_2 (flow rate = 1200 mL min^{-1}), H_2O vapor = 0.5 mol%, 25°C , 4 h; hydrogenation: $\text{H}_2 = 60 \text{ mL min}^{-1}$, 1.0 MPa, 320°C for 2.5 h (5°C min^{-1}).

^a Heating rate at 5°C min^{-1} during hydrogenation of captured CO_2 . ^b Heating rate of $20^\circ\text{C min}^{-1}$ during hydrogenation of captured CO_2 .

^c Average diameter is not given due to low surface area.

Along with CO_2 , CH_4 also formed and was the highest when the temperature reached 320°C as shown in Fig. 1B. C_2H_4 and C_2H_6 were also produced at Region 1 (at 320°C , 2.5 h). Further increasing the temperature to 360°C resulted in additional CH_4 production along with small amounts of ethylene and ethane (Fig. 1D). Overall, ~74% of the total captured CO_2 was converted to C_1 and C_2 products with ~94.4% selectivity to methane, 4.2% selectivity to ethane, and 1.4% selectivity to ethene. To the best of our knowledge, this is the first demonstration for conversion of captured CO_2 (air derived) to C_1 and C_2 based products in the presence of an Fe-based catalyst. Besides the formation of olefins, which are the target products, the production of renewable methane from the captured CO_2 is also advantageous. This presents an alternative pathway for generating synthetic natural gas, and its utilization in existing infrastructure could lead to a lower carbon footprint. There were no detectable amounts of higher olefins or paraffins formed. Decreasing the heating rate from 20 to 5°C min^{-1} decreased the overall conversion of CO_2 along with a decrease in olefin selectivity at 320°C (Fig. 1C). Increasing the hydrogen pressure further increased the selectivity to methane with a

decrease in the conversion of the captured CO_2 (see Fig. 1C and D).

A decrease in CO_2 capture with $\text{K}_2\text{CO}_3/\text{Fe/C}$ compared to $\text{K}_2\text{CO}_3/\text{Al}_2\text{O}_3$ is likely due to the smaller surface area of Fe/C ($33.16 \text{ m}^2 \text{ g}^{-1}$), which results in larger K_2CO_3 particles (Table 1). A lower CO_2 loading could inhibit C–C bond formation because there are fewer carbons. To increase the surface area and eventually improve the capture performance, $\text{K}_2\text{CO}_3/\text{Fe/C/Al}_2\text{O}_3$ was synthesized *via* the wet impregnation method, as discussed in section S1.2,† and the adsorption capacity was compared with that of $\text{K}_2\text{CO}_3/\text{Al}_2\text{O}_3$ and $\text{K}_2\text{CO}_3/\text{Fe/C}$ under similar capture conditions. The capture performance was significantly improved after the addition of Al_2O_3 . The $\text{K}_2\text{CO}_3/\text{Fe/C/Al}_2\text{O}_3$ captured ~1220 $\mu\text{mol g}^{-1}$ of CO_2 (vs. 600–700 $\mu\text{mol g}^{-1}$ of CO_2 for $\text{K}_2\text{CO}_3/\text{Fe/C}$) (Fig. 2A). This difference can be explained from the BET results of the support over which K_2CO_3 was impregnated. The BET isotherms of three materials are shown in Fig. 3A. Dispersion of K_2CO_3 on Al_2O_3 retained the mesoporosity of the support and showed a type IV isotherm despite a decrease in the surface area as shown in Table 1. The isotherm of Fe/C is a type II isotherm with no pro-

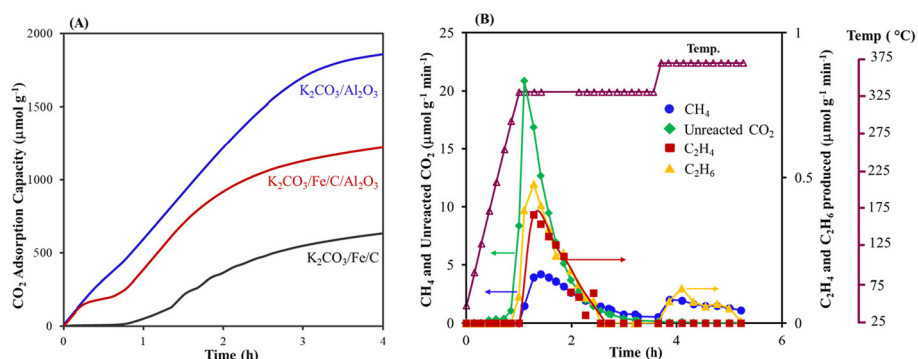


Fig. 2 (A) Comparison of the CO_2 adsorption capacity of K_2CO_3 on various materials pretreated at 400°C under H_2 flow, and (B) hydrogenation of the captured CO_2 over $\text{K}_2\text{CO}_3/\text{Fe/C/Al}_2\text{O}_3$ at 320°C and 360°C . Amount of material: 2 g; pretreatment conditions: $\text{H}_2 = 60 \text{ mL min}^{-1}$, 400°C , 5 h ($\text{K}_2\text{CO}_3/\text{Al}_2\text{O}_3$) and 10 h ($\text{K}_2\text{CO}_3/\text{Fe/C/Al}_2\text{O}_3$ and $\text{K}_2\text{CO}_3/\text{Fe/C}$); CO_2 capture conditions: $\text{CO}_2 = 400 \text{ ppm}$ in N_2 (flow rate = 1200 mL min^{-1}), H_2O vapor = 0.5 mol%, 25°C , 4 h; hydrogenation: $\text{H}_2 = 60 \text{ mL min}^{-1}$, 1.0 MPa, 320°C for 2.5 h (5°C min^{-1}), followed by heating to 360°C (5°C min^{-1}) for 2 h. The selectivity of CO is <5% during the hydrogenation.



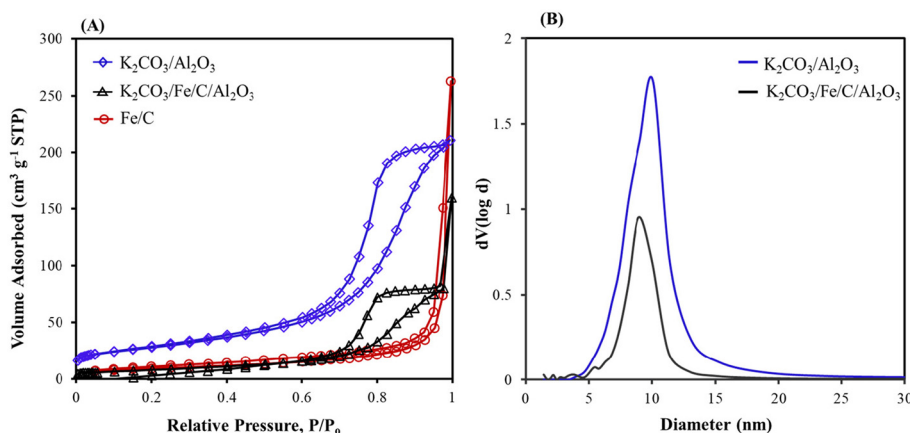


Fig. 3 (A) Nitrogen adsorption–desorption isotherms of K_2CO_3/Al_2O_3 , $K_2CO_3/Fe/C/Al_2O_3$, and Fe/C and (B) Barrett–Joyner–Halenda (BJH) curves for K_2CO_3/Al_2O_3 , and $K_2CO_3/Fe/C/Al_2O_3$.

nounced hysteresis loop, showing that the material is either non-porous or microporous. The surface area is very low compared to the Al_2O_3 support and has no pores, as shown in Table 1. Therefore, the impregnation of K_2CO_3 could have formed larger particles on Fe/C , leading to lower CO_2 capture.⁴⁹ Due to the presence of the Al_2O_3 pores, K_2CO_3 was well dispersed over a mixture of high-surface-area, mesoporous Al_2O_3 and non-porous Fe/C . This led to higher CO_2 capture for $K_2CO_3/Fe/C/Al_2O_3$ compared to only $K_2CO_3/Fe/C$, as shown in Table 1.

With the improvement in capture performance, the CO_2 captured in $K_2CO_3/Fe/C/Al_2O_3$ was converted *in situ* (Fig. 2B shows the conversion profile of captured CO_2). A comparison of the conversion activities of $K_2CO_3/Fe/C$ and $K_2CO_3/Fe/C/Al_2O_3$ is shown in Table 1. Interestingly, the C_2 – C_4 olefin selectivity significantly improved to 7.3% in the case of $K_2CO_3/Fe/C/Al_2O_3$. The improved C–C coupled products formation could be because of the relatively high CO_2 loading. In addition, a small amount of C_5^+ products (~1%) was also detected. Increasing the hydrogenation temperature to 360 °C increased the conversion and selectivity further to methane. Increased methane formation at higher temperature could be due to a decrease in the chain growth probability of the

Anderson–Schultz–Flory product distribution that governs the FTS reaction.⁶¹ Alternatively, it could be due to less carbon (*i.e.*, captured CO_2) content on the material, which could prevent C–C formation.

Fe/ K_2CO_3/Al_2O_3 and Fe–Co/ K_2CO_3/Al_2O_3 . Because the physical mixture of Fe_2O_3 – K_2CO_3/Al_2O_3 formed no CO_2 hydrogenation products, we prepared Fe– K_2CO_3/Al_2O_3 (Fe/KA) and Fe–Co/ K_2CO_3/Al_2O_3 (Fe–Co/KA) (by incipient wetness impregnation of Fe and Co salts on K_2CO_3/Al_2O_3) to improve the cooperativity between Fe and K to produce C–C coupled products. After pretreating these materials at 400 °C for 5 h under H_2 flow, the CO_2 capture was performed under standard conditions (400 ppm of CO_2 , 0.5 mol% of H_2O vapor, 25 °C, 4 h). The Fe–Co/KA captured 1970 $\mu\text{mol g}^{-1}$ of CO_2 , which is almost similar to K_2CO_3/Al_2O_3 (pretreated at 400 °C), showing that the addition of the catalytic component (Fe) had no impact on the capture performance. Hydrogenation of the captured CO_2 using Fe–Co/KA was carried out at two different temperature ramp rates, 5 and 20 °C min^{-1} . Increasing the heating rate decreased the CO_2 conversion to value-added products with no significant impact on product distribution, as shown in Table 2.

Table 2 Comparison of CO_2 capture and conversion performance for Fe–Co/KA and Fe/KA at 320 °C

	Heating rate (°C min^{-1})	CO_2 captured ($\mu\text{mol g}^{-1}$)	CO_2 conv. (%)	Selectivity to hydrocarbons		
				CH ₄ sel (%)	C_2 – C_4 paraffins sel (%)	C_2 – C_4 olefins sel (%)
Fe–Co/KA	5	1970	21.3	88.3	5.1	6.7
	20	1970	12.0	86.8	8.3	4.9
Fe/KA	5	1645	22.4	79.7	8.9	11.4
Fe/KA ^a	5	1525	18.1	81.9	6.6	11.5
Fe/KA (H ₂ /CO pretreated) ^b	5	1659	24.5	72.1	11.2	16.7

Amount of material: 2 g; pretreatment conditions: H_2 = 60 mL min^{-1} , 400 °C, 5 h; CO_2 capture conditions: CO_2 = 400 ppm in N_2 (flow rate = 1200 mL min^{-1}), H_2O vapor = 0.5 mol%, 25 °C, 4 h; hydrogenation: H_2 = 60 mL min^{-1} , 1.0 MPa, 320 °C for 2.5 h (5 °C min^{-1}). The selectivity of CO is <5% during the hydrogenation. ^a CO_2 capture conditions: CO_2 = 430 ppm CO_2 (in 78% nitrogen, 21% oxygen and <1% other gases).

^b Pretreatment conditions: H_2/CO (2 : 1) = 60 mL min^{-1} , 400 °C, 3 h, followed by H_2 = 60 mL min^{-1} , 400 °C, 5 h.



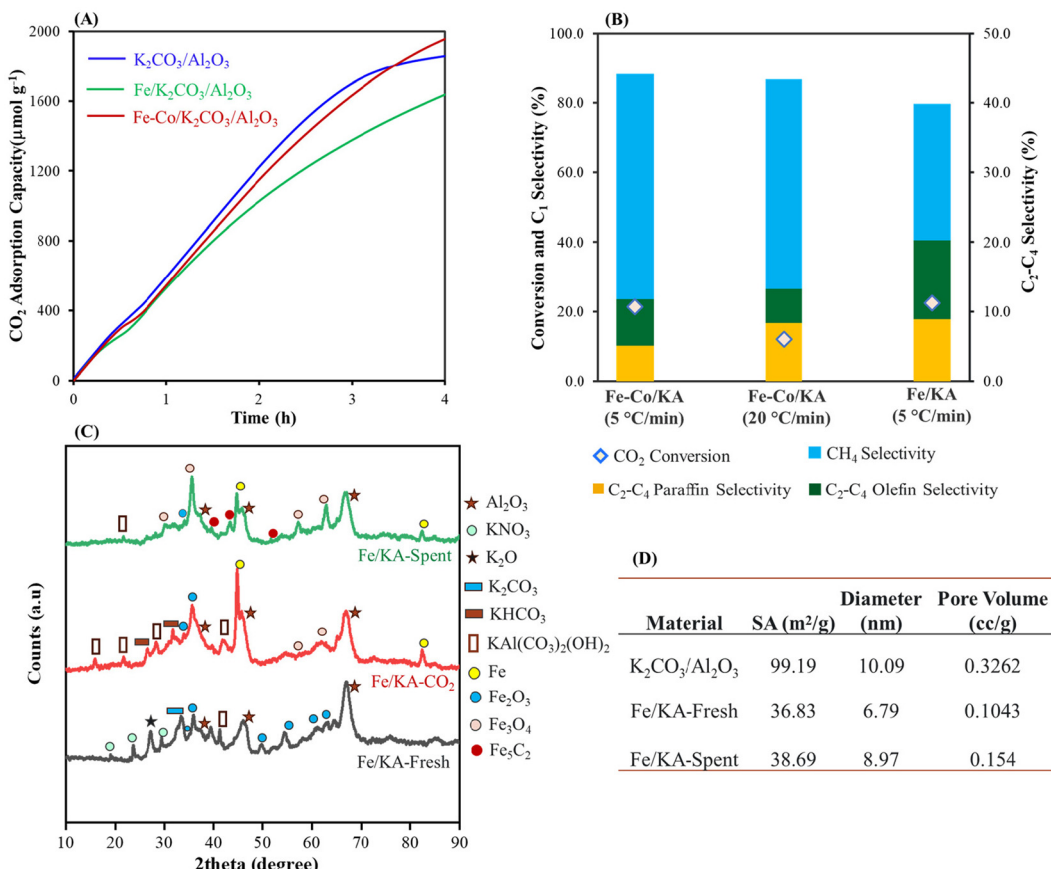


Fig. 4 (A) Comparison of CO₂ adsorption capacity of K₂CO₃/Al₂O₃, Fe-Co/KA and Fe/KA, (B) comparison of hydrogenation of Fe-Co/KA with different heating rates and Fe/KA (C) X-ray diffraction patterns of fresh, CO₂ captured and spent Fe/KA, and (D) physicochemical properties of the K₂CO₃/Al₂O₃ and Fe/KA materials. Amount of material: 2 g; pretreatment conditions: H₂ = 60 mL min⁻¹, 400 °C, 5 h; CO₂ capture conditions: CO₂ = 400 ppm in N₂ (flow rate = 1200 mL min⁻¹), H₂O vapor = 0.5 mol%, 25 °C, 4 h; hydrogenation: H₂ = 60 mL min⁻¹, 1.0 MPa, 320 °C for 2.5 h (5 °C min⁻¹). The selectivity of CO is <5% during the hydrogenation.

The Fe/KA captured ~1600 μmol g⁻¹ of CO₂ at our standard capture conditions as shown in Fig. 4A. The hydrogenation results are shown in Fig. S5A† and Table 2. At 320 °C, C₂-C₄ olefins and paraffins started forming accompanied with the formation of CH₄. The highest olefin selectivity of ~11.4% was obtained with a CO₂ conversion of 22.4% as shown in Fig. 4B. Next, to understand the effect of oxygen on the capture and conversion, CO₂ capture was performed with real air (430 ppm CO₂ containing 21% oxygen) using Fe/KA, which captured ~1500 μmol g⁻¹ of CO₂. After the CO₂ capture, the material was purged with N₂ for 10 min to remove air. The subsequent hydrogenation produced C₂-C₄ olefins with a selectivity of 11.5% and a CO₂ conversion of 18.1%, suggesting that the presence of oxygen during capture did not significantly affect the conversion and selectivity.

The BET isotherm shows that the mesoporosity of the K₂CO₃/Al₂O₃ is still maintained after impregnation of Fe particles (Fig. S5B†). Upon impregnating Fe, the surface area decreased from 99.19 (for K₂CO₃/Al₂O₃) to 36.83 m² g⁻¹ and the diameter of the mesopores decreased to 6.79 nm, confirming the formation of Fe particles inside the mesopores (Fig. 4D).

The average pore size of the spent Fe/KA material (after hydrogenation) increased compared to the fresh material along with slight increase in the pore volume and surface area. This shows that after the hydrogenation, more dispersed particles were formed. This could be due to the formation of Fe₅C₂ and Fe₃O₄ particles during the high-temperature hydrogenation.

Fig. 4C shows wide-angle XRD of the fresh Fe/KA, CO₂ captured Fe/KA and spent (after hydrogenation) Fe/KA. In the fresh sample, diffraction peaks corresponding to KNO₃, dawsonite, and Fe₂O₃ particles were evident. XRD of the CO₂-captured Fe/KA material shows peaks for KHCO₃ and dawsonite along with some Fe₂O₃ and Fe particles. The Fe particles could form from Fe₂O₃ due to hydrogenation with H₂ at high temperature.⁶² The spent (after hydrogenation) Fe/KA shows peaks for Fe₅C₂ along with Fe₃O₄, which were formed during hydrogenation of the captured CO₂. The formation of these dispersed particles resulted in an increase of pore volume and of the average pore size of the material. The formation of the Fe₅C₂ phase shows the carburization of Fe₃O₄ particles.

The spent Fe/KA after the first cycle of capture and hydrogenation was reused to study the robustness of these materials



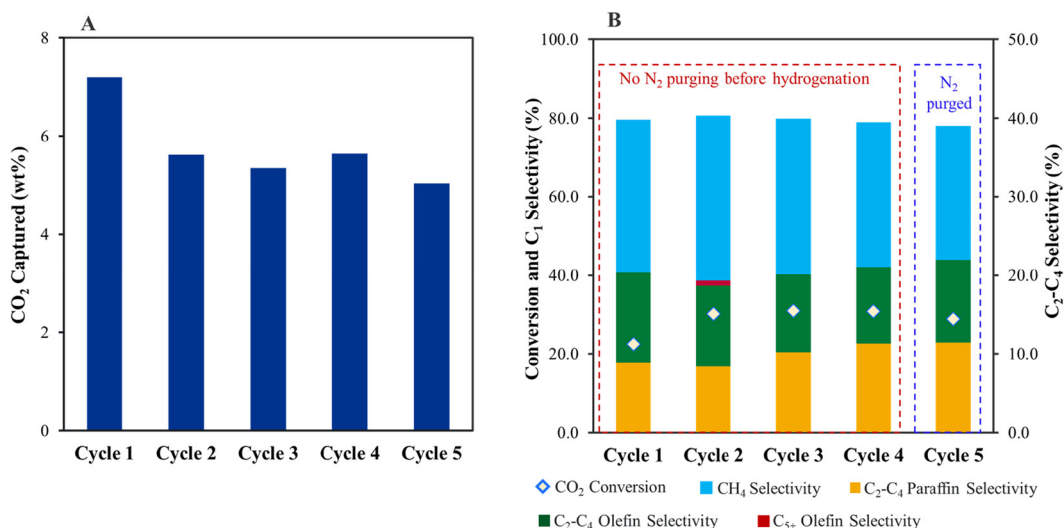


Fig. 5 (A) CO₂ capture and (B) hydrogenation of captured CO₂ over five cycles using Fe/KA. Fe/KA: 2 g, pretreatment conditions: H₂ = 60 mL min⁻¹, 400 °C, 5 h; CO₂ capture conditions: CO₂ = 400 ppm in N₂ (flow rate = 1200 mL min⁻¹), H₂O vapor = 0.5 mol%, 25 °C, 4 h; hydrogenation: H₂ = 60 mL min⁻¹, 1.0 MPa, 320 °C for 2.5 h (5 °C min⁻¹) followed by heating to 400 °C (5 °C min⁻¹) for 2.5 h to mimic the pretreatment conditions. For cycle 5, the spent catalyst was purged with N₂ (30 mL min⁻¹) for 1 h before hydrogenation. The selectivity of CO is <5% during the hydrogenation.

(Fig. 5). The capture capacity was reduced in the second cycle to 1276 $\mu\text{mol g}^{-1}$ (5.6 wt% CO₂) compared to 1645 $\mu\text{mol g}^{-1}$ (7.4 wt% CO₂) in the first cycle. However, the capture performance was steady in the subsequent third (5.4 wt%), fourth (5.6 wt%), and fifth (~5.03 wt%) cycles. The drop in the capture capacity could be because of the presence of K₂O in the fresh Fe/KA, which consumed CO₂ from air to form K₂CO₃. A similar drop in the capture capacity was observed between the first (6.5 wt% CO₂) and second cycles (5.3 wt% CO₂) for K₂CO₃/Al₂O₃ (Table S3†). However, in this case (K₂CO₃/Al₂O₃), the drop in performance could be because the low-temperature pretreatment conditions (at 200 °C for 1 h) prevented the conversion of dawsonite back to K₂CO₃. Prior to hydrogenation during the fifth cycle, the CO₂ captured material was purged with N₂ flow for 1 h to quantify physiosorbed CO₂ content. Only trace amounts of CO₂ were released during the N₂ purge, and subsequent hydrogenation showed consistent conversion and selectivity to products, demonstrating that the material is stable for at least five cycles.

To understand the effect of the CO₂ : H₂ ratio and reaction temperature on the product distribution and conversion, the

gas-phase hydrogenation studies were performed with Fe/KA using 1 : 3 and 1 : 10 ratios of CO₂ : H₂. The conversion results for the Fe/KA at 320 °C and 360 °C are shown in Tables 3 and 4, along with Fig. 6. At 320 °C, in the case of the 1 : 10 ratio of CO₂/H₂, the selectivity to C₂-C₄ paraffins was higher compared to DAC and 1 : 3 ratio of CO₂/H₂ studies. The O/P (olefin/paraffin) ratio selectivity to C₂-C₄ olefins was not significantly altered by the CO₂/H₂ ratio at 320 °C. In addition to C₂-C₄ products, C₅+ products were detected by gas chromatography in the case of 1 : 3 ratio of CO₂/H₂. The reaction temperature played a significant role in O/P selectivity and CO₂ conversion. The CO₂ conversion was 66% and 15% for 1 : 10 and 1 : 3 ratios of CO₂/H₂, respectively, at 360 °C (Table 4). High olefin selectivity and O/P (olefin/paraffin) ratios were achieved for 1 : 3 ratio of CO₂/H₂ at 360 °C. In addition, the CO selectivity depends on the reaction temperature and the CO₂ : H₂ ratio. As shown in Tables 3 and 4, a higher temperature (*i.e.*, 360 °C) and lower CO₂ concentrations significantly reduced the CO selectivity, suggesting that the reaction is proceeding *via* the CO intermediate.

Table 3 Comparison of hydrogenation of captured CO₂ with gas-phase CO₂ at 320 °C over Fe/KA

	Selectivity of hydrocarbons (%)							
	CO ₂ conv. (%)	CO sel (%)	CH ₄ sel (%)	C ₂ -C ₄ paraffins sel (%)	C ₂ -C ₄ olefins sel (%)	C ₅ + olefins (sel %)	C ₅ + (sel %)	O/P ratio
DAC	22.4	<5	79.7	8.9	11.4	0.0	0.0	1.3
CO ₂ : H ₂ = 1 : 10	22	54.7	33.5	33.1	24.2	9.21	0.0	0.73
CO ₂ : H ₂ = 1 : 3	9.55	79.4	33.4	22.5	36.6	6.91	0.50	1.62

Fe/KA = 2 g, amount of material: 2 g; pretreatment conditions: H₂ = 60 mL min⁻¹, 400 °C, 5 h; CO₂ capture conditions: CO₂ = 400 ppm in N₂ (flow rate = 1200 mL min⁻¹), H₂O vapor = 0.5 mol%, 25 °C, 4 h; hydrogenation: H₂ = 60 mL min⁻¹, 1.0 MPa, 320 °C for 2.5 h (5 °C min⁻¹); CO₂ : H₂ = 1 : 10 or 1 : 3 ratio; flow rate = 60 mL min⁻¹, 1.0 MPa, 320 °C for 2.5 h (5 °C min⁻¹); GHSV = 1800 mL h⁻¹ g⁻¹.



Table 4 Comparison of hydrogenation of gas-phase CO_2 at 360 °C over Fe/KA

	CO_2 conv. (%)	CO sel (%)	Selectivity of hydrocarbons (%)					O/P ratio
			CH ₄ sel (%)	$\text{C}_2\text{-C}_4$ paraffins sel (%)	$\text{C}_2\text{-C}_4$ olefins sel (%)	C_{5+} olefins (sel %)	C_{5+} (sel %)	
$\text{CO}_2 : \text{H}_2 = 1 : 10$	66.0	11.5	49.5	8.19	36.4	5.27	0.61	4.5
$\text{CO}_2 : \text{H}_2 = 1 : 3$	14.7	37.3	34.4	6.97	48.0	9.17	1.40	6.9

Fe/KA = 2 g, pretreatment conditions: $\text{H}_2 = 60 \text{ mL min}^{-1}$, 400 °C, 5 h; $\text{CO}_2 : \text{H}_2 = 1 : 10$ or $1 : 3$ ratio; flow rate = 60 mL min^{-1} , 1.0 MPa, 320 °C for 2.5 h ($5 \text{ }^\circ\text{C min}^{-1}$) followed by heating to 360 °C ($5 \text{ }^\circ\text{C min}^{-1}$) for 2 h; GHSV = $1800 \text{ mL h}^{-1} \text{ g}^{-1}$.

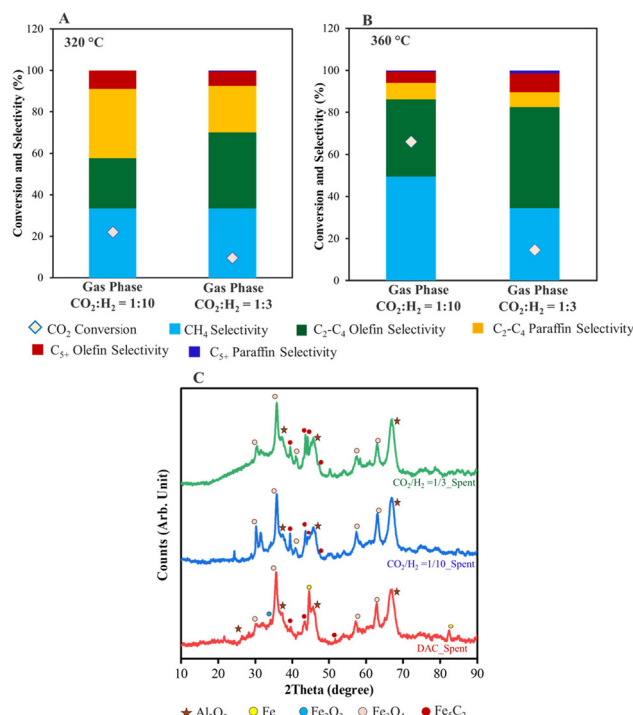


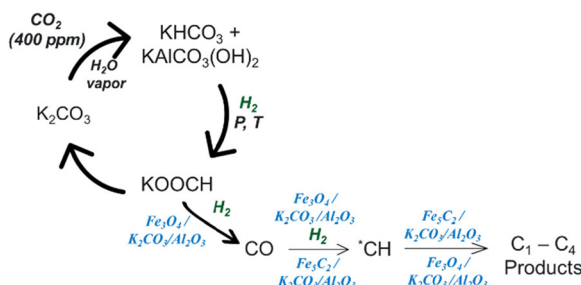
Fig. 6 Comparison of gas-phase hydrogenation at (A) 320 °C and (B) 360 °C using Fe/KA. (C) Comparison of XRD of Fe/KA for DAC and gas-phase reactions carried out at 1:10 and 1:3 ratios of $\text{CO}_2 : \text{H}_2$. Reaction Conditions: Fe/KA: 2 g, total flow rate = 60 mL min^{-1} , $\text{CO}_2 : \text{H}_2 = 1 : 10$ or $1 : 3$ ratios; flow rate = 60 mL min^{-1} , 1.0 MPa, 320 °C for 2.5 h ($5 \text{ }^\circ\text{C min}^{-1}$), followed by heating to 360 °C for 2 h ($5 \text{ }^\circ\text{C min}^{-1}$); GHSV = $1800 \text{ mL h}^{-1} \text{ g}^{-1}$.

The XRD spectra of the spent DAC and gas-phase CO_2 hydrogenation materials are shown in Fig. 6C. Fe_3O_4 was observed in all spent materials. The Fe_5C_2 diffraction patterns are more pronounced for the 1:3 CO_2/H_2 reaction compared to the 1:10 CO_2/H_2 reaction. This agrees with the decreased CH_4 selectivity and increased O/P ratio of the 1:3 CO_2/H_2 reaction because both Fe_3O_4 (for the RWGS) and Fe_5C_2 are important for C–C formation (Table 4). Peaks for Fe were also observed in the spent DAC material, showing that not all of the Fe was carburized to Fe_5C_2 . The formation of the carbide-phase reaction route is as follows: $\text{Fe}_2\text{O}_3 \rightarrow \text{Fe}_3\text{O}_4 \rightarrow \text{FeO} \rightarrow \text{Fe}$, and then finally the Fe is carburized to Fe_5C_2 .⁶³

The Fourier transform infrared spectroscopy (FTIR) spectrum of the spent DAC and gas-phase CO_2 hydrogenation materials were compared (Fig. S6†). The C–H vibrations were seen between 2960 – 2627 cm^{-1} corresponding to formate and other bound –CH species. The carbonyl vibration of formate was observed at the $\sim 1631 \text{ cm}^{-1}$ region.⁶⁴ The Fe–CO interactions were visible in the 1800 – 2100 cm^{-1} region, which corresponds to bound CO with different forms of Fe.⁶⁵ In addition to formate and CO, there are additional bands visible for carbonates and bicarbonates in the IR spectrum.

To further enhance the formation of C–C coupled products, we pretreated the Fe/KA with an H_2/CO gas mixture to improve iron carbide formation. The outlet gas stream during the pretreatment consisted of CO_2 , CH_4 and $\text{C}_2\text{-C}_4$ hydrocarbons. After H_2/CO pretreatment, Fe/KA was treated with H_2 at 400 °C to remove CO_2 and other hydrocarbons adsorbed on the Fe/KA prior to CO_2 capture. The capture capacity of this H_2/CO pretreated Fe/KA was $1659 \mu\text{mol g}^{-1}$ at our standard CO_2 capture conditions, which is comparable to Fe/KA (Table 2). Subsequent hydrogenation of the captured CO_2 resulted in an enhancement in C–C coupled products selectivity to 27.9% (16.7% selectivity to $\text{C}_2\text{-C}_4$ olefins and 11.2% selectivity to $\text{C}_2\text{-C}_4$ paraffins) with a slight improvement in the CO_2 conversion to 24.5%. The selectivity of the hydrogenated products for the first hour at 320 °C is shown in Fig. S7.† It is evident that the selectivity to C–C coupled products was high, $\sim 50\%$ (with $>30\%$ selectivity to $\text{C}_2\text{-C}_4$ olefins), initially, but decreased significantly as the concentration of the captured CO_2 decreased.

Based on the selectivity of the products and the XRD and FTIR analyses of the spent samples, the conversion of captured CO_2 to olefins occurs through the direct CO_2 conversion pathway, where the CO_2 is converted to CO via the RWGS in the presence of Fe_3O_4 .⁶⁶ Subsequently, the CO is converted to C–C products following the FTS mechanism in the presence of Fe_5C_2 .⁶⁶ A proposed pathway has been shown in Scheme 1. When CO_2 (400 ppm) is captured in the presence of water vapor at room temperature, the K_2CO_3 of Fe/KA transforms into KHCO_3 and $\text{KAlCO}_3(\text{OH})_2$. This transformation leads to the formation of HCOOK and CO upon hydrogenation catalyzed by $\text{Fe}_3\text{O}_4/\text{KA}$. The $\text{Fe}_3\text{O}_4/\text{KA}$ is derived from $\text{Fe}_2\text{O}_3/\text{KA}$ in the presence of H_2 . Furthermore, the $\text{Fe}_3\text{O}_4/\text{KA}$ facilitates the conversion of CO to $^*\text{CH}$ species, which undergo C–C coupling in the presence of Fe_5C_2 formed *in situ* during the reaction. The increased selectivity observed for the C–C coupled pro-



Scheme 1 Proposed mechanism for the conversion of captured CO_2 to C–C coupled products in the presence of Fe/KA.

ducts (as depicted in Table 2 and Fig. S7†) following the pretreatment of Fe/KA with H_2/CO gas mixture strongly suggests that the enhanced formation of Fe_5C_2 facilitates C–C coupling.

A preliminary techno-economic analysis (TEA) and life-cycle analysis (LCA) were conducted to evaluate the proposed iDAC-CAT technology for olefins production. In both TEA and LCA, it was assumed that renewable hydrogen, electri-

city, and fossil-based natural gas were used as main energy inputs. A process model was developed in Aspen Plus V14 to calculate the mass and energy balance and life-cycle inventory of the proposed technology based on the performance measures and assumptions listed in Table 5. The results were compared with NETL's case study for sorbent-based DAC⁶⁷ and other CO_2 to olefin technologies available in the literature.⁶⁸

Fig. 7 shows the process flow diagram of the technology, where air first enters the adsorption bed, and CO_2 is adsorbed by the sorbent at ambient conditions. The bed is then heated to 320 °C and H_2 is fed to the bed to produce CH_4 and olefins from CO_2 . The product stream leaving the adsorption bed contains H_2 , CH_4 , and C_{2+} olefins. H_2 is first separated in the pressure swing adsorption (PSA) unit. The remaining products are then sent to a de-methanization tower. This tower is of the design commonly used in the commercial ethylene plants, and operated at cryogenic conditions (−100 °C, 35 bar). The CH_4 and C_{2+} olefin streams from the tower are depressurized and then used to pre-chill the inlet stream. In the TEA, the plant size was set the same as Case 0B in the NETL's case study for sorbent-based DAC.⁶⁷ The capital cost of the iDAC-CAT unit was calculated by adjusting NETL Case 0B value⁶⁷ based on flowrate and cycling time. The capital cost of the downstream product separation and purification section was calculated using Aspen Process Economic Analyzer V14. A simple annualized cost approach was used to calculate the minimum olefin selling price with 20-year depreciation and 10% per year return on investment. It was assumed that the renewable natural gas (RNG) produced as by-product can be sold at a price of \$13 per MMBtu,⁶⁹ roughly five times of the market price of fossil-based natural gas. For the Fe/KA material, CatCostTM tool⁷⁰ was used to estimate its production cost as a pre-commercial material as well as the utility consumptions and emissions during the manufacturing step. For the LCA, a cradle-to-gate system boundary was used to evaluate the life-cycle greenhouse gases (GHG) emissions of olefin production using the iDAC-CAT technology, which was compared with conventional petrochemical process. The functional unit

Table 5 Technology performance measures and assumptions for TEA and LCA

Assumptions	Value	Assumptions	Value
Adsorption temperature (°C)	25	Conversion temperature (°C)	320
Adsorption pressure (bar)	1	Conversion pressure (bar)	10
Adsorption time (hr)	2	Conversion time with heating (hr)	2
CO_2 capture (%)	62	CO_2 conversion (%)	80
Sorbent loading (wt% CO_2)	5	C_{2+} olefin selectivity (%)	60
Plant size (tonne CO_2 per year)	100 000	CH_4 selectivity (%)	40
H_2 Price (\$ per kg)	5	Excess hydrogen (ratio over stoic)	4

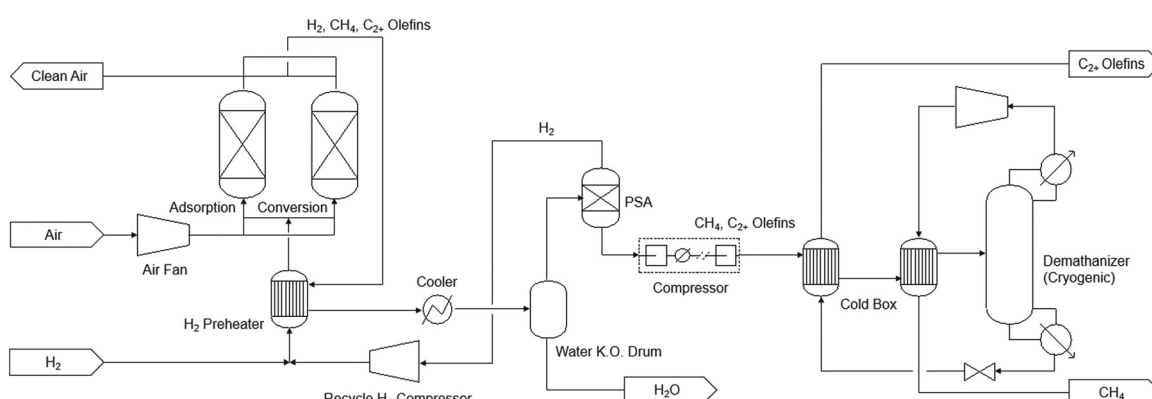


Fig. 7 Process flow diagram of the proposed integrated DAC-CAT technology for olefins production.



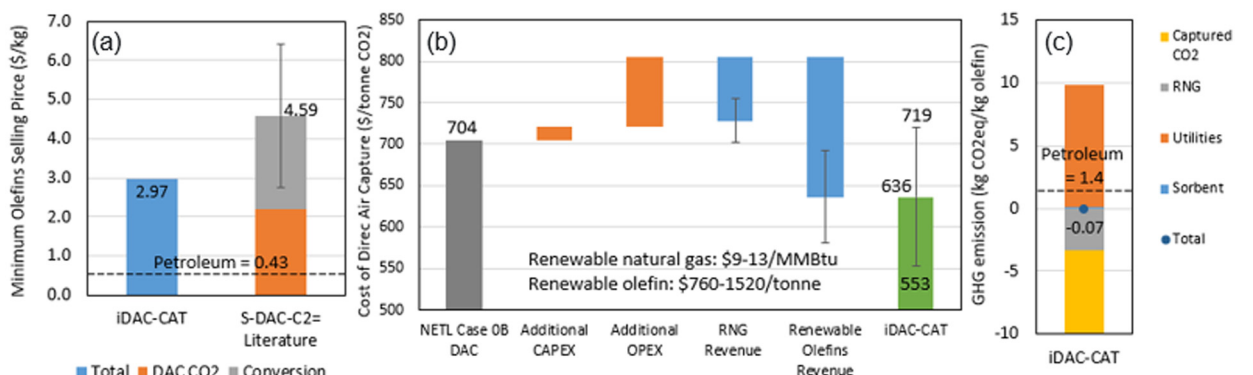


Fig. 8 Economic and environmental performance: (a) minimum olefin selling price; (b) cost of direct air capture; (c) life-cycle GHG emissions.

Table 6 Mass and Energy Balance and life-cycle inventory for the iDAC-CAT process

	Mass energy balance	Life cycle inventory	Carbon intensity
Products			
C_{2+} olefins	2360 kg h^{-1}		
RNG	2015 kg h^{-1}	$-0.045 \text{ MMBtu kg}^{-1} C_{2+}$ olefins	$72.62 \text{ kg CO}_2 \text{ eq. MMBtu}^{-1} \text{ NG}$
Feedstock			
Renewable H ₂	2112 kg h^{-1}	$0.895 \text{ kg kg}^{-1} C_{2+}$ olefins	$0 \text{ kg CO}_2 \text{ eq. kg}^{-1} H_2$
CO ₂ captured	$15\,553 \text{ kg h}^{-1}$	$6.590 \text{ kg kg}^{-1} C_{2+}$ olefins	$-1 \text{ kg CO}_2 \text{ eq. kg}^{-1} CO_2$
Sorbent (Fe/KA)	116 kg h^{-1}	$0.049 \text{ kg kg}^{-1} C_{2+}$ olefins	$2.20 \text{ kg CO}_2 \text{ eq. kg}^{-1}$ sorbent
Utilities			
Electricity	$32\,984 \text{ kW}$	$13.98 \text{ kW h kg}^{-1} C_{2+}$ olefins	$0 \text{ kg CO}_2 \text{ eq. kW}^{-1} h^{-1}$ electricity
NG	$315.3 \text{ MMBtu h}^{-1}$	$0.133 \text{ MMBtu kg}^{-1} C_{2+}$ olefins	$72.62 \text{ kg CO}_2 \text{ eq. MMBtu}^{-1} \text{ NG}$

was set to per kg of olefins produced. Carbon Intensity data for each raw material and energy involved in the process were sourced from the GREET 2022⁷¹ and Ecoinvent V3.8 databases.

The preliminary TEA and LCA results were summarized in Fig. 8, while the mass and energy balance, life-cycle inventory and carbon intensity were provided in Table 6. Fig. 8(a) suggests the integrated iDAC-CAT technology can potentially produce renewable olefins at a cost 35% lower than that of a separated DAC and CO₂ to olefins (S-DAC-C₂=) technology.^{67,68} Fig. 8(b) indicates that the iDAC-CAT technology can significantly reduce the cost of DAC on a per tonne CO₂ basis. The error bars in both Fig. 8(a) and (b) represent the uncertainties in TEA results from literature, as well as the market prices of RNG and olefins. Furthermore, Fig. 8(c) and Table 6 demonstrate that the CO₂ adsorbed from the atmosphere and the GHG emissions avoided by producing RNG can completely offset the GHG emissions from upstream processes and the iDAC-CAT process when renewable H₂ is used as a process input. A GHG emission reduction of 105% can be achieved compared to the petroleum baseline.

Conclusions

A series of materials have been evaluated for direct air capture and conversion to C-C coupled products for the first time. A novel multifunctional and multicomponent material for

iDAC-CAT has been developed, employing a combination of non-noble metal and solid inorganic sorbent, Fe/K₂CO₃/Al₂O₃. Upon the impregnation of catalytic Fe particles to the sorbent (K₂CO₃/Al₂O₃), despite the decrease in surface area, pore size, and pore volume, high and consistent CO₂ capture was realized at room temperature in presence of water vapor. This shows that the addition of Fe particles did not significantly change the CO₂ capture property of K₂CO₃/Al₂O₃. On recycling, the material showed a consistent capture capacity of ~5 wt% for up to five cycles, followed by consistent CO₂ conversion into C-C products. In contrast, the physical mixture of Fe₂O₃ and K₂CO₃/Al₂O₃ desorbed the CO₂ and showed no formation of C₁-C₄ products on hydrogenation. Based on this comparison and activity data of various combination of materials, along with XRD and BET results, it is evident that the proximity between the Fe and K on the Al₂O₃ is important for CO₂ activation and subsequent conversion to C-C products.

We have successfully developed an approach for integrated direct air capture and conversion to C-C coupled products using Fe/K₂CO₃/Al₂O₃. The utilization of this material for CO₂ capture from the air and subsequent conversion to C₂₊ products represents an environmentally friendly approach. Despite the current breakthrough and success of the bench-scale experiment, scaling up poses multiple risks. Factors such as kinetics, material mechanical strength and stability, environmental conditions throughout the year, processing temperature range, and deployment site must be carefully con-



sidered during the scaling process. Our preliminary TEA analysis indicates that iDAC-CAT technology has the potential to substantially decrease the cost of DAC. The preliminary LCA suggests a 105% reduction in GHG emissions compared to the petroleum baseline, and indicates a negative cradle-to-gate GHG emission for renewable olefin production *via* iDAC-CAT when renewable H₂ is used as the process input. Future efforts will focus on developing materials with enhanced reactivity for C–C coupling and stronger CO₂ binding affinity to prevent desorption during conversion at the high temperatures required for C–C coupling reactions. Further exploration of Fe/K₂CO₃/Al₂O₃ under varying conditions, and experimentation with different material combinations, is needed to improve the conversion efficiency. This exploration should be accompanied by a full TEA and LCA to assess its feasibility for real-world applications.

Author contributions

Shazia Sharmin Satter: investigation, data curation, and writing – original draft; Johnny Saavedra Lopez: investigation, methodology, and writing – editing, Michael L. Hubbard: investigation and data curation, Yuan Jiang: TEA, LCA and writing – editing, Robert A. Dagle: conceptualization, and writing – editing; Jotheeswari Kothandaraman: supervision, funding acquisition, conceptualization, investigation, data curation, and writing – review and editing.

Conflicts of interest

There are no conflicts to declare.

Acknowledgements

This work was supported by the Laboratory Directed Research and Development Program (LDRD) at Pacific Northwest National Laboratory (PNNL). The authors would like to thank Dr Jaelynne A. King and Dr Austin D. Winkelman for performing the FTIR and XRD measurements, respectively. The Pacific Northwest National Laboratory is proudly operated by Battelle for the US Department of Energy.

References

- 1 J. Hilaire, J. C. Minx, M. W. Callaghan, J. Edmonds, G. Luderer, G. F. Nemet, J. Rogelj and M. del Mar Zamora, *Clim. Change*, 2019, **157**, 189–219.
- 2 W. J. Shaw, M. K. Kidder, S. R. Bare, M. Delferro, J. R. Morris, F. M. Toma, S. D. Senanayake, T. Autrey, E. J. Biddinger, S. Boettcher, M. E. Bowden, P. F. Britt, R. C. Brown, R. M. Bullock, J. G. Chen, C. Daniel, P. K. Dorhout, R. A. Efroymson, K. J. Gaffney, L. Gagliardi, A. S. Harper, D. J. Heldebrant, O. R. Luca, M. Lyubovsky, J. L. Male, D. J. Miller, T. Prozorov, R. Rallo, R. Rana, R. M. Rioux, A. D. Sadow, J. A. Schaidle, L. A. Schulte, W. A. Tarpeh, D. G. Vlachos, B. D. Vogt, R. S. Weber, J. Y. Yang, E. Arenholz, B. A. Helms, W. Huang, J. L. Jordahl, C. Karakaya, K. C. Kian, J. Kothandaraman, J. Lercher, P. Liu, D. Malhotra, K. T. Mueller, C. P. O'Brien, R. M. Palomino, L. Qi, J. A. Rodriguez, R. Rousseau, J. C. Russell, M. L. Sarazen, D. S. Sholl, E. A. Smith, M. B. Stevens, Y. Surendranath, C. J. Tassone, B. Tran, W. Tumas and K. S. Walton, *Nat. Rev. Chem.*, 2024, **8**, 376–400.
- 3 P. M. Bhatt, Y. Belmabkhout, A. Cadiou, K. Adil, O. Shekhah, A. Shkurenko, L. J. Barbour and M. Eddaoudi, *J. Am. Chem. Soc.*, 2016, **138**, 9301–9307.
- 4 D. G. Boer, J. Langerak and P. P. Pescarmona, *ACS Appl. Energy Mater.*, 2023, **6**, 2634–2656.
- 5 P. Murge, S. Dinda and S. Roy, *Langmuir*, 2019, **35**, 14751–14760.
- 6 R. V. Siriwardane, M.-S. Shen, E. P. Fisher and J. A. Poston, *Energy Fuels*, 2001, **15**, 279–284.
- 7 S. A. Didas, S. Choi, W. Chaikittisilp and C. W. Jones, *Acc. Chem. Res.*, 2015, **48**, 2680–2687.
- 8 W. Chaikittisilp, H.-J. Kim and C. W. Jones, *Energy Fuels*, 2011, **25**, 5528–5537.
- 9 N. G. McQueen, K. V. McCormick, C. Blumanthal, K. Pisciotta and M. Wilcox, *J. Prog. Energy*, 2021, **3**, 032001.
- 10 M. A. Sabri, S. Al Jitan, D. Bahamon, L. F. Vega and G. Palmisano, *Sci. Total Environ.*, 2021, **790**, 148081.
- 11 D. J. Heldebrant, J. Kothandaraman, N. M. Dowell and L. Brickett, *Chem. Sci.*, 2022, **13**, 6445–6456.
- 12 R. E. Siegel, S. Pattanayak and L. A. Berben, *ACS Catal.*, 2022, **13**, 766–784.
- 13 S. Kar, A. Goeppert and G. K. S. Prakash, *Acc. Chem. Res.*, 2019, **52**, 2892–2903.
- 14 J. Kothandaraman, A. Goeppert, M. Czaun, G. A. Olah and G. K. Prakash, *J. Am. Chem. Soc.*, 2016, **138**, 778–781.
- 15 N. M. Rezayee, C. A. Huff and M. S. Sanford, *J. Am. Chem. Soc.*, 2015, **137**, 1028–1031.
- 16 J. B. Jakobsen, M. H. Ronne, K. Daasbjerg and T. Skrydstrup, *Angew. Chem., Int. Ed.*, 2021, **60**, 9174–9179.
- 17 S. Kar, J. Kothandaraman, A. Goeppert and G. K. S. Prakash, *J. CO₂ Util.*, 2018, **23**, 212–218.
- 18 X. Shi, H. Xiao, H. Azarabadi, J. Song, X. Wu, X. Chen and K. S. Lackner, *Angew. Chem., Int. Ed.*, 2020, **59**, 6984–7006.
- 19 R. Custelcean, *Annu. Rev. Chem. Biomol. Eng.*, 2022, **13**, 217–234.
- 20 J. Kothandaraman, J. S. Lopez, Y. Jiang, E. D. Walter, S. D. Burton, R. A. Dagle and D. J. Heldebrant, *Adv. Energy Mater.*, 2022, **12**(46), 2202369.
- 21 J. Kothandaraman, J. S. Lopez, Y. Jiang, E. D. Walter, S. D. Burton, R. A. Dagle and D. J. Heldebrant, *ChemSusChem*, 2021, **14**, 4812–4819.
- 22 J. Kothandaraman, A. Goeppert, M. Czaun, G. A. Olah and G. K. S. Prakash, *Green Chem.*, 2016, **18**, 5831–5838.
- 23 D. Wei, H. Junge and M. Beller, *Chem. Sci.*, 2021, **12**, 6020–6024.



24 S. Jo, H. D. Son, T.-Y. Kim, J. H. Woo, D. Y. Ryu, J. C. Kim, S. C. Lee and K. L. Gilliard-AbdulAziz, *Chem. Eng. J.*, 2023, **469**, 143772.

25 T. Sasayama, F. Kosaka, Y. Liu, T. Yamaguchi, S.-Y. Chen, T. Mochizuki, A. Urakawa and K. Kuramoto, *J. CO₂ Util.*, 2022, **60**, 102049.

26 M. S. Duyar, M. A. A. Treviño and R. J. Farrauto, *Appl. Catal., B*, 2015, **168–169**, 370–376.

27 L. Hu and A. Urakawa, *J. CO₂ Util.*, 2018, **25**, 323–329.

28 M. Abdallah, Y. C. Y. Lin and R. Farrauto, *Appl. Catal., B*, 2023, **339**, 123105.

29 C. Jeong-Potter, M. Abdallah, C. Sanderson, M. Goldman, R. Gupta and R. Farrauto, *Appl. Catal., B*, 2022, **307**, 120990.

30 C. Jeong-Potter and R. Farrauto, *Appl. Catal., B*, 2021, **282**, 119416.

31 C. Jeong-Potter, M. A. Arellano-Treviño, W. W. McNeary, A. J. Hill, D. A. Ruddy and A. T. To, *EES Catal.*, 2024, **2**, 253–261.

32 J. Pazdera, E. Berger, J. A. Lercher and A. Jentys, *Catal. Commun.*, 2021, **159**, 106347.

33 J. Pazdera, D. Issayeva, J. Titus, R. Gläser, O. Deutschmann and A. Jentys, *ChemCatChem*, 2022, **14**, e202200620.

34 L. C. Wirner, F. Kosaka, T. Sasayama, Y. Liu, A. Urakawa and K. Kuramoto, *Chem. Eng. J.*, 2023, **470**, 144227.

35 A. Bermejo-López, B. Pereda-Ayo, J. A. González-Marcos and J. R. González-Velasco, *J. CO₂ Util.*, 2019, **34**, 576–587.

36 F. Kosaka, Y. Liu, S.-Y. Chen, T. Mochizuki, H. Takagi, A. Urakawa and K. Kuramoto, *ACS Sustainable Chem. Eng.*, 2021, **9**, 3452–3463.

37 S. C. Lee, H. J. Chae, S. J. Lee, B. Y. Choi, C. K. Yi, J. B. Lee, C. K. Ryu and J. C. Kim, *Environ. Sci. Technol.*, 2008, **42**, 2736–2741.

38 M. S. Cho, S. C. Lee, H. J. Chae, Y. M. Kwon, J. B. Lee and J. C. Kim, *Process Saf. Environ. Prot.*, 2018, **117**, 296–306.

39 S. B. Jo, S. C. Lee, H. J. Chae, M. S. Cho, J. B. Lee, J.-I. Baek and J. C. Kim, *Korean J. Chem. Eng.*, 2016, **33**, 3207–3215.

40 J. Holladay, Z. Abdullah and J. Heyne, *Technical Report: Sustainable Aviation Fuel: Review of Technical Pathways*, United States, 2020, doi: DOI: [10.2172/1660415](https://doi.org/10.2172/1660415).

41 E. S. Sanz-Perez, C. R. Murdock, S. A. Didas and C. W. Jones, *Chem. Rev.*, 2016, **116**, 11840–11876.

42 J. Wang, L. Huang, R. Yang, Z. Zhang, J. G. Wu, Y. Gao, Q. Wang, D. O'Hare and Z. Zhong, *Energy Environ. Sci.*, 2014, **7**, 3478–3518.

43 J. V. Veselovskaya, V. S. Derevschikov, T. Y. Kardash and A. G. Okunev, *Renew. Bioresour.*, 2015, **3**, 1.

44 J. V. Veselovskaya, V. S. Derevschikov, T. Y. Kardash, O. A. Stonkus, T. A. Trubitsina and A. G. Okunev, *Int. J. Greenhouse Gas Control*, 2013, **17**, 332–340.

45 A. G. Okunev, V. E. Sharonov, Y. I. Aristov and V. N. Parmon, *React. Kinet. Catal. Lett.*, 2000, **71**, 355–362.

46 V. E. Sharonov, E. A. Tyshchishchin, E. M. Moroz, A. G. Okunev and Y. I. Aristov, *Russ. J. Appl. Chem.*, 2001, **74**, 409–413.

47 J. V. Veselovskaya, V. S. Derevschikov, A. S. Shalygin and D. A. Yatsenko, *Microporous Mesoporous Mater.*, 2021, **310**, 110624.

48 M. Yan, Y. Zhang, Q. Huan, Y. Song, X. Zhou, H. Wibowo and C. Yu, *Biomass Convers. Biorefin.*, 2022, **14**, 3667–3677.

49 N. Masoud, G. Bordanaba-Florit, T. v. Haasterecht and J. H. Bitter, *Ind. Eng. Chem. Res.*, 2021, **60**, 13749–13755.

50 C. Zhao, X. Chen and C. Zhao, *Energy Fuels*, 2009, **23**, 4683–4687.

51 S. C. Lee, H. J. Chae, B. Y. Choi, S. Y. Jung, C. Y. Ryu, J. J. Park, J.-I. Baek, C. K. Ryu and J. C. Kim, *Korean J. Chem. Eng.*, 2011, **28**, 480–486.

52 J. V. Veselovskaya, A. I. Lysikov, O. V. Netskina, D. V. Kuleshov and A. G. Okunev, *Ind. Eng. Chem. Res.*, 2020, **59**, 7130–7139.

53 J. Kothandaraman, J. S. Lopez, Y. Jiang, E. D. Walter, S. D. Burton, R. A. Dagle and D. J. Heldebrant, *Adv. Energy Mater.*, 2022, **12**, 2202369.

54 D. Wang, Z. H. Xie, M. D. Porosoff and J. G. G. Chen, *Chem.*, 2021, **7**, 2277–2311.

55 T. Numpilai, N. Chanlek, Y. Poo-Arporn, C. K. Cheng, N. Siri-Nguan, T. Sornchamni, M. Chareonpanich, P. Kongkachuichay, N. Yigit, G. Rupprechter, J. W. Limtrakul and T. Witoon, *ChemCatChem*, 2020, **12**, 3306–3320.

56 A. Ramirez, S. Ould-Chikh, L. Gevers, A. D. Chowdhury, E. Abou-Hamad, A. Aguilar-Tapia, J. L. Hazemann, N. Wehbe, A. J. Al Abdulghani, S. M. Kozlov, L. Cavallo and J. Gascon, *ChemCatChem*, 2019, **11**, 2879–2886.

57 Y. Han, C. Fang, X. Ji, J. Wei, Q. Ge and J. Sun, *ACS Catal.*, 2020, **10**, 12098–12108.

58 C. G. Visconti, M. Martinelli, L. Falbo, A. Infantes-Molina, L. Lietti, P. Forzatti, G. Iaquaniello, E. Palo, B. Picutti and F. Brignoli, *Appl. Catal., B*, 2017, **200**, 530–542.

59 H. Yu, C. Wang, T. Lin, Y. An, Y. Wang, Q. Chang, F. Yu, Y. Wei, F. Sun, Z. Jiang, S. Li, Y. Sun and L. Zhong, *Nat. Commun.*, 2022, **13**, 5987.

60 J. Ren, N. Ai, D. Ou and Y. Yu, *Mol. Catal.*, 2023, **538**, 112990.

61 H. M. T. Galvis and K. P. de Jong, *ACS Catal.*, 2013, **3**, 2130–2149.

62 J. Zieliński, I. Zglinskia, L. Znak and Z. Kaszkur, *Appl. Catal., A*, 2010, **381**, 191–196.

63 V. V. Ordovsky, B. Legras, K. Cheng, S. Paul and A. Y. Khodakov, *Catal. Sci. Technol.*, 2015, **5**, 1433–1437.

64 J. Lee and J. Otomo, *Ind. Eng. Chem. Res.*, 2023, **62**, 12096–12108.

65 V. I. Bogdan, A. E. Koklin, A. L. Kustov, Y. A. Pokusaeva, T. V. Bogdan and L. M. Kustov, *Molecules*, 2021, **26**, 2883.

66 B. Pawelec, R. Guil-Lopez, N. Mota, J. L. G. Fierro and R. M. Navarro Yerga, *Materials*, 2021, **14**, 6952.

67 J. Valentine and A. Zoelle, *Direct Air Capture Case Studies: Sorbent System*, DOE/NETL-2021/2865, National Energy Technology Laboratory, 2022, DOI: [10.2172/1879535](https://doi.org/10.2172/1879535).

68 A. Somoza-Tornos, O. J. Guerra, A. M. Crow, W. A. Smith and B. M. Hodge, *iScience*, 2021, **24**, 102813.



69 R. Gupta, Reactive CO₂ Capture DAC-DFM, *ARPA-E Reactive Carbon Capture Workshop*, 2022.

70 <https://catcost.chemcatbio.org/home>.

71 M. Wang, A. Elgowainy, U. Lee, K. H. Baek, A. Bafana, P. T. Benavides, A. Burnham, H. Cai, V. Cappello, P. Chen, Y. Gan, U. R. Gracida-Alvarez, T. R. Hawkins, R. K. Iyer,

J. C. Kelly, T. Kim, S. Kumar, H. Kwon, K. Lee, X. Liu, Z. Lu, F. H. Masum, C. Ng, L. Ou, K. Reddi, N. Siddique, P. Sun, P. Vyawahare, H. Xu and G. G. Zaimes, *Summary of Expansions and Updates in GREET® 2022*, ANL/ESIA-22/1, Argonne National Laboratory, 2022.

